

Communication

# Electrocatalytic Enhancement of CO Methanation at the Metal–Electrolyte Interface Studied Using In Situ X-ray Photoelectron Spectroscopy

Christoph W. Thurner <sup>1,†</sup>, Leander Haug <sup>1,†</sup>, Daniel Winkler <sup>1,†</sup>, Christoph Griesser <sup>1</sup>, Matthias Leitner <sup>1</sup>, Toni Moser <sup>1</sup>, Daniel Werner <sup>1</sup>, Marco Thaler <sup>1</sup>, Lucas A. Scheibel <sup>1</sup>, Thomas Götsch <sup>2</sup>, Emilia Carbonio <sup>2,3</sup>, Julia Kunze-Liebhäuser <sup>1</sup>, Engelbert Portenkirchner <sup>1</sup>, Simon Penner <sup>1</sup> and Bernhard Klötzer <sup>1,\*</sup>

- <sup>1</sup> Institute of Physical Chemistry, University of Innsbruck, Innrain 52c, A-6020 Innsbruck, Austria; christoph.thurner@uibk.ac.at (C.W.T.); leander.haug@uibk.ac.at (L.H.); d.winkler@uibk.ac.at (D.W.); christoph.griesser@uibk.ac.at (C.G.); m.leitner@uibk.ac.at (M.L.); toni.moser@uibk.ac.at (T.M.); daniel.werner@uibk.ac.at (D.W.); marco.thaler@uibk.ac.at (M.T.); lucas.scheibel@student.uibk.ac.at (L.A.S.); julia.kunze@uibk.ac.at (J.K.-L.); engelbert.portenkirchner@uibk.ac.at (E.P.); simon.penner@uibk.ac.at (S.P.)
- <sup>2</sup> Fritz-Haber Institute of the Max-Planck Society, Department of Inorganic Chemistry, Faradayweg 4–6, 14195 Berlin, Germany; goetsch@fhi-berlin.mpg.de (T.G.); carbonio@fhi-berlin.mpg.de (E.C.)
- <sup>3</sup> Catalysis for Energy, Energy Materials In Situ Laboratory (EMIL), Helmholtz-Zentrum Berlin für Materialien und Energie GmbH, BESSY II, Albert-Einstein-Straße 15, 12489 Berlin, Germany
- \* Correspondence: bernhard.kloetzer@uibk.ac.at
- † These authors contributed equally to this work.

**Abstract:** For the direct reduction of CO<sub>2</sub> and H<sub>2</sub>O in solid oxide electrolysis cells (SOECs) with cermet electrodes toward methane, a fundamental understanding of the role of elemental carbon as a key intermediate within the reaction pathway is of eminent interest. The present synchrotron-based in situ near-ambient-pressure X-ray photoelectron spectroscopy (NAP-XPS) study shows that alloying of Ni/yttria-stabilized-zirconia (YSZ) cermet electrodes with Cu can be used to control the electrochemical accumulation of interfacial carbon and to optimize its reactivity toward CO<sub>2</sub>. In the presence of syngas, sufficiently high cathodic potentials induce excess methane on the studied Ni/yttria-stabilized-zirconia (YSZ)-, NiCu/YSZ- and Pt/gadolinium-doped-ceria (GDC) cermet systems. The hydrogenation of carbon, resulting from CO activation at the triple-phase boundary of Pt/GDC, is most efficient.

**Keywords:** SOEC; methanation; electrocatalysis; NAP-XPS



**Citation:** Thurner, C.W.; Haug, L.; Winkler, D.; Griesser, C.; Leitner, M.; Moser, T.; Werner, D.; Thaler, M.; Scheibel, L.A.; Götsch, T.; et al. Electrocatalytic Enhancement of CO Methanation at the Metal–Electrolyte Interface Studied Using In Situ X-ray Photoelectron Spectroscopy. *C* **2023**, *9*, 106. <https://doi.org/10.3390/c9040106>

Academic Editors: Małgorzata Zakrzewska and Ana S. Reis-Machado

Received: 11 October 2023  
Revised: 25 October 2023  
Accepted: 3 November 2023  
Published: 8 November 2023



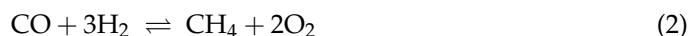
**Copyright:** © 2023 by the authors. Licensee MDPI, Basel, Switzerland. This article is an open access article distributed under the terms and conditions of the Creative Commons Attribution (CC BY) license (<https://creativecommons.org/licenses/by/4.0/>).

## 1. Introduction

The co-electrolysis of CO<sub>2</sub> (g) and water to methane (reaction (1)) in high-temperature SOECs is a process that could help to mitigate issues related to climate change by utilizing the main greenhouse gas for electric energy storage in the form of a renewable energy carrier [1,2]:



The most common reaction pathway does not realize reaction (1) directly, as it deals with the simultaneous electrochemical reduction of CO<sub>2</sub> to CO and H<sub>2</sub>O to H<sub>2</sub>. The resulting CO/H<sub>2</sub> syngas mixture can be utilized to form a variety of hydrocarbons. For this, an adjustable CO/H<sub>2</sub> ratio is required, e.g., 1:3 to form methane (reaction (2)).



Based on thermodynamics, temperatures up to ~673 K are beneficial for CO methanation [3]. In this study, we (i) provide a proof-of-principle that reactive carbon species are formed particularly on Ni(Cu)/8 mol% yttria-stabilized-zirconia (8-YSZ) cermets via

electrolysis of CO, and (ii) show that additional methane is formed generally on metal–electrolyte interfaces such as Ni(Cu)/8-YSZ and Pt/10 mol% Gd-doped-ceria (GDC-10), even at high temperatures (~973 K), via electrocatalytic promotion of CO methanation. An additional non-faradaic influence (i.e., change in the metal’s work function and adsorbate chemistry) on the catalytic reaction, according to the concept of “electrochemical promotion of catalysis” (EPOC) or “non-faradaic electrochemical modification of catalytic activity” (NEMCA) [4–6], is deliberately surpassed by choosing special experimental conditions, i.e., high temperatures, resulting in a high oxygen ion conductivity, and high potentials, resulting in high current densities, leading to the dominance of faradaic effects [5–7].

In the co-electrolysis of CO<sub>2</sub> and H<sub>2</sub>O, surface carbon chemistry plays a major role. Carbon can be deposited via different pathways, involving electrochemical (reaction (3)) or conventional thermal reduction of CO (reaction (4)), Boudouard reaction (5)). Commonly, these pathways are held responsible for surface coking and blocking of the triple-phase-boundary (TPB) [8,9].



Vice versa, de-coking can proceed via the inverse reactions of (3)–(5) or, alternatively, via the reaction of carbon with co-generated hydrogen from electrochemical water splitting to form methane (reverse CH<sub>4</sub> pyrolysis reaction (6)):



How reactive the material- and site-specific deposited carbon species are is crucial, for both the efficiency of de-coking and of direct hydrocarbon formation. In other words, equilibrium (6) imposes the need for a distinction between reactive *intermediate* and site-blocking *side product* carbon forms [10]. The carbon reactivity argument holds equally for the reversal of reaction (1), which needs to be realized for direct methane SOFCs [11,12].

For the electrochemical promotion of CH<sub>4</sub> synthesis according to reaction (2), both the kinetic reactivity and the chemical potential of carbon formed directly at the TPB via reaction (3) are essential. Bimetallic electrode materials, which allow for directional modulation of the bond strength and adsorption properties of carbon species [13], can be applied to electrochemically generated carbon, denoted as C<sub>TPB</sub> in the following, and are the key toward a knowledge-based reactivity control. Ni<sub>x</sub>Cu<sub>y</sub> is considered a promising alloy, fulfilling these carbon-chemistry-related requirements [14,15]. Moreover, it features decreased carbon solubility, which is essential for the suppression of unreactive graphene/graphitic deposits [16,17]. However, considering the thermo-catalytic methanation reaction of CO or CO<sub>2</sub>, NiCu-alloyed catalysts perform worse than Ni [18–20]. Nonetheless, it is important to note that alongside the hydrogenation of intermediate C, the rate-limiting step is the dissociation of CO or CO<sub>2</sub> [21,22]. The latter can be promoted by means of electrochemistry (reaction (3)). As a result, it enables the utilization of electrocatalyst materials beyond the current scientific boundaries.

Taking the thermodynamic equilibrium constant  $K$  of reaction (6) into account, the carbon activity  $a(\text{C})$  influences the equilibrium pressure  $p$  of CH<sub>4</sub>:

$$K = \frac{p(\text{CH}_4)}{a(\text{C}) \cdot p(\text{H}_2)^2} \quad (7)$$

If additional carbon is induced electrochemically via reaction (3) in a H<sub>2</sub>-containing atmosphere, the methane yield can be enhanced both by increasing the carbon activity via increasing the cathodic polarization, and by increasing the H<sub>2</sub> pressure [23]. Of course, the efficiency of the latter in terms of thermodynamic promotion of CH<sub>4</sub> yield is limited by the kinetics of reaction (6). In the following, a comparative approach, with respect to (i) the

$C_{\text{TPB}}$  growth and clean-off on Ni/8-YSZ vs.  $\text{Ni}_{80}\text{Cu}_{20}$ /8-YSZ working electrodes (WE) and (ii) the  $C_{\text{TPB}}$ -promoted formation of methane on Ni(Cu)/8-YSZ (WE) vs. Pt/GDC-10 counter electrodes (CE), is presented. Therefore, a “triple” in situ combination of electrochemical biasing, product detection via online mass spectrometry (MS), and near-ambient-pressure X-ray photoelectron spectroscopy (NAP-XPS) was employed, which allows us to study the surface carbon chemistry of the electrochemical active Ni(Cu)/8-YSZ interface as a function of bias, while utilizing online tracking for product formation and recording in situ XP spectra. This extended and novel combination of experimental in situ techniques represents a considerably more powerful approach to studying surface processes in solid oxide cells under close-to-real reaction conditions.

To ensure the comparability of the carbon-active WE (i.e., Ni/8-YSZ vs.  $\text{Ni}_{80}\text{Cu}_{20}$ /8-YSZ), the cell dimensions and the manufacturing of electrolyte and CE were kept exactly the same. The CE benefits are associated with the specific cermet material properties (i.e., Pt and GDC), being electrocatalytically highly active toward oxygen exchange reactions (GDC) and  $\text{H}_2$  activation (Pt) [24].

However, with respect to the CO methanation reaction rate (i.e.,  $C_{\text{TPB}}$ -promoted formation of methane), Pt is prone to be more than four orders of magnitude less active than the WE metal Ni under otherwise identical conditions [25]. Based on the pronounced difference in the CO methanation activity of Ni and Pt, the chosen setup allows us to allocate the electrochemically driven formation of additional methane (beyond the purely thermocatalytic  $\text{CH}_4$  formation rate induced by the Ni side) to the CE or WE side, respectively. As the formation of extra carbon via CO electrolysis is only possible under cathodic polarization conditions on either side via reaction (3), separated electrode compartments are not necessary to allocate the source of the extra  $\text{CH}_4$  formed via reaction (6).

## 2. Experimental Methods

The investigation of the interfacial carbon chemistry at defined atmospheres over cermet WEs was carried out via in situ near-ambient-pressure X-ray photoelectron spectroscopy (NAP-XPS) at the ISSS end station at the BESSY II synchrotron facility. This setup allows us to measure XPS at elevated pressures (up to 7 mbar) and X-ray energies from 80 to 2000 eV. The surface-sensitive XP-spectra were recorded with photon energies which correspond to a photo electron energy of 150 eV and therefore equal information depth.

For the synthesis of the WE, a Ni(Cu)/8-YSZ cermet powder was prepared via a precipitation impregnation method, where Ni(Cu) was precipitated as hydroxide onto an aqueous suspension of YSZ powder. A subsequent oxidative (He:O<sub>2</sub> 1:1, 1123 K, 3 h) and reductive treatment (He:H<sub>2</sub> 5:1, 1073 K, 2 h) yields the final cermet powder. The cell stack was assembled by pressing the CE cermet powder (Pt/GDC-10), the electrolyte powder 8-YSZ, and the WE cermet powder (Ni(Cu)/8-YSZ) into a button cell (diameter 10 mm). After sintering in a He:H<sub>2</sub> (5:1) mixture at 1523 K for 3 h, the final cell was obtained. For a detailed description of the cell preparation, sample mounting, equipment, and XPS data analysis [26–28], we refer to the supporting information (Figure S1).

## 3. Results and Discussion

### 3.1. Carbon-Active Electrodes

To highlight the difference in the carbon reactivity at the interface, visible in the kinetics of carbon growth and clean-off reactions, in situ XP spectra of the C 1s region of the Ni/8-YSZ and  $\text{Ni}_{80}\text{Cu}_{20}$ /8-YSZ electrodes were recorded at 973 K (Figure 1). In the order of the spectra from bottom to top, we initially applied 0.5 mbar CO at open circuit potential (OCP) to the electrode and detected a minor amount of mixed carbon-oxygenates and elemental carbon species in the C1s region (i.e., components are assigned to  $\text{O}-\text{C}=\text{O}_{\text{ads}}$ ,  $\text{C}=\text{O}_{\text{ads}}$ ,  $\text{C}-\text{O}-\text{C}_{\text{ads}}$ , and  $\text{C}-\text{C}_{\text{ads}}$  species). As the Boudouard reaction (5) is strongly shifted toward CO formation under the chosen experimental conditions, we observed hardly any growth of the C1s signals after 15 min of isothermal exposure. Upon applying a voltage of  $-1.5$  V, graphitic-like  $C_{\text{TPB}}$  at a BE of 284.7 eV can be electrochemically grown via reaction (3).

However, the terminology “ $C_{TPB}$ ” species means that the spectroscopically observed graphitic-like species is fed by electrolysis of CO at the TPB. Inherently, this implies a transition from an atomic to a graphitic-like carbon state.

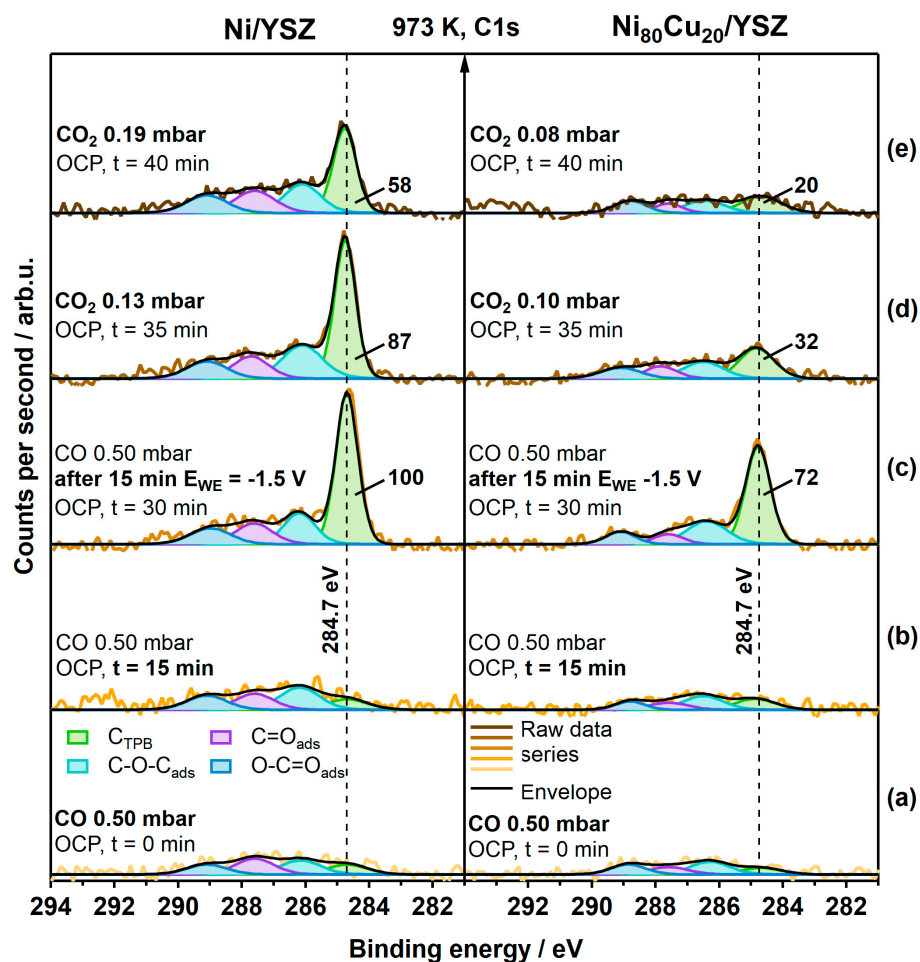


**Figure 1.** In situ XPS spectra series of the C 1s region recorded on the Ni/8-YSZ and Ni<sub>80</sub>Cu<sub>20</sub>/8-YSZ WE at 973 K under the following conditions (from bottom to top): (a) 0.500 mbar CO, OCP; (b) 0.500 mbar CO, OCP, after 15 min; (c) 0.500 mbar CO, OCP, after 15 min  $-1.5$  V; (d) 0.13 mbar CO<sub>2</sub> for Ni/8-YSZ and 0.10 mbar CO<sub>2</sub> for Ni<sub>80</sub>Cu<sub>20</sub>/8-YSZ, both at OCP; (e) 0.19 mbar CO<sub>2</sub> and 0.08 mbar CO<sub>2</sub> for the respective electrode.

After 15 min of CO electrolysis, the  $C_{TPB}$  growth was terminated by returning to OCP and CO pump-off. To study the efficiency of the oxidative clean-off reaction of this carbon species (reversal of reaction (5)), the electrode was then exposed to 0.13 mbar pure CO<sub>2</sub> under OCP conditions. For Ni/8-YSZ (left panel in Figure 1), only a slow decrease in the  $C_{TPB}$  component of  $\sim 13\%$  toward  $\sim 87\%$  of the initial value was observed after 5 min exposure. By increasing the CO<sub>2</sub> partial pressure up to 0.19 mbar and an exposure for an additional 5 min, a further, but still rather slow, decrease in the  $C_{TPB}$  peak area to  $\sim 58\%$  of the initial value was achieved. To compare such carbon clean-off rates with the NiCu system, the peak area of the largest graphitic-like  $C_{TPB}$  component was normalized to 100%.

In contrast, the amount of analogously grown  $C_{TPB}$  on the Ni<sub>80</sub>Cu<sub>20</sub>/8-YSZ electrode (right side in Figure 1), starting with an initial relative intensity of  $\sim 72\%$ , is diminished by  $\sim 40\%$  toward  $\sim 44\%$  at a CO<sub>2</sub> pressure of 0.10 mbar after 5 min. After another 5 min (topmost spectra), the  $C_{TPB}$  peak started to vanish (i.e., 20% residual intensity), although the CO<sub>2</sub> partial pressure was kept at an even lower value of 0.08 mbar. By comparing the relative carbon clean-off rates of the graphitic-like  $C_{TPB}$  on Ni vs. NiCu, a pronounced

difference in the initial decrease in the relative integral  $C_{\text{TPB}}$  peak areas within the first 5 min was found (i.e.,  $-13\%$  for Ni and  $-40\%$  for  $\text{Ni}_{80}\text{Cu}_{20}$ ). These results indicate that graphitic-like  $C_{\text{TPB}}$  is more reactive for the oxidative carbon clean-off reaction (5) on the  $\text{Ni}_{80}\text{Cu}_{20}/8\text{-YSZ}$  electrode. To achieve a better resolution of the carbon clean-off reaction as a function of time, slightly different  $\text{CO}_2$  partial pressures were deliberately chosen, as a more pronounced activity of the NiCu electrode was anticipated.

To confirm that carbon is accumulated via the TPB onto the cermet surface, XP spectra series (Figure S2) of Cu 2p, Ni 2p, C 1s, and Zr 3d were recorded before and after electrochemically-induced carbon growth, showing a decrease in the cermet components. The Ni/Cu ratio in Figure S2 changed from 2.95 before carbon growth toward 5.40 thereafter. Whether this change is a consequence of an alteration of the Ni to Cu surface composition upon electrochemically-induced adsorbate chemistry [29], or if it is due to preferential carbon covering of Ni surface area/sites, or a geometric shielding effect of Cu vs. Ni areas on the porous electrode structure, remains open.

To elucidate the  $C_{\text{TPB}}$  reactivity toward  $\text{H}_2$  on Ni/8-YSZ and  $\text{Ni}_{80}\text{Cu}_{20}/8\text{-YSZ}$ , the reaction mixture was changed to 0.125 mbar CO and 0.375 mbar  $\text{H}_2$  (total pressure 0.5 mbar; CO: $\text{H}_2$  ratio = 1:3). The XP spectra of the C 1s region shown in Figure 2, recorded in situ at 973 K, show no carbon growth at open-circuit-potential (OCP). After applying a cathodic potential of  $-1.0$  V for 30 min on either system, a graphitic-like  $C_{\text{TPB}}$ -related peak appears only on the  $\text{Ni}_{80}\text{Cu}_{20}/8\text{-YSZ}$  electrode ( $\text{BE} \approx 284.7$  eV). According to literature there are pronounced differences regarding the carbon bulk solubility on NiCu (low) vs. pure Ni (high) [16] and the carbon clean-off with  $\text{H}_2$  (reaction (6)) on NiCu (low) vs. Ni (high) [20]. These material/catalytic properties confirm the result of a hampered segregation, especially of  $C_{\text{TPB}}$  on Ni, and a more pronounced accumulation of graphitic-like carbon (resulting from  $C_{\text{TPB}}$ ) at the NiCu surface. This raises the question of whether this additional carbon species is kinetically available at all for enhanced methane formation through reaction (6). Equilibrium thermodynamics generally favor the reversal of (6) at increasing temperatures [3], but can be counteracted by the law of mass action (7), which predicts increasing methane pressures with increasing carbon activity  $a(\text{C})$ . In turn,  $a(\text{C})$  can be varied via polarization through equilibrium (3). Figure S3 in the supporting information provides the respective calculated equilibrium partial pressures of  $\text{CH}_4$  at 973 K as a function of  $a(\text{C})$ , based on data from [30].

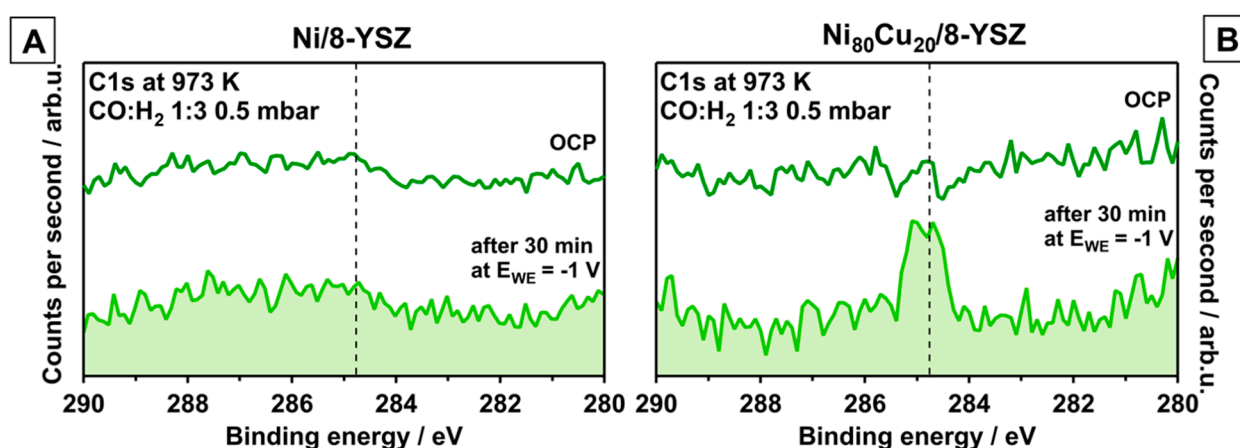


**Figure 2.** C1s XP-spectra recorded in situ at 973 K in 0.500 mbar CO: $\text{H}_2$  = 1:3 atmosphere at  $t = 0$  s at OCP and after  $-1.00$  V was applied to the working electrode for 30 min (dark and light green traces, respectively). Panel (A,B) compare electrochemically-induced  $C_{\text{TPB}}$  growth on Ni/8-YSZ vs.  $\text{Ni}_{80}\text{Cu}_{20}/8\text{-YSZ}$  (vertical dashed line).

Mechanistically, we suggest at least three different reaction pathways for  $C_{\text{TPB}}$ :

- (a) Clean-off reaction with  $H_{\text{ads}}$  toward  $\text{CH}_4$ , which is a function of the available active hydrogen species;
- (b) Dissolution of C atoms in the (bi)metal bulk;
- (c) Accumulation of graphitic-like carbon.

Pathways (a) and (b) are disfavored on NiCu according to [16,20] as compared to Ni, therefore explaining the observed accumulation of graphitic-like carbon on NiCu via pathway (c).

### 3.2. Electrochemically Promoted Methane Formation

In principle, the promotion of  $a(\text{C})$  through reaction (3) via cathodic polarization can increase  $\text{CH}_4$  formation thermodynamically through equilibrium (7). Whether the kinetics are in favor of a faster methanation or not depends on the reactivity of the specific TPB sites, the  $\text{H}_2$ -reducibility of the electrolytically generated carbonaceous species, and the influence of a potential EPOC effect at the metal.

Cyclo-voltammetry (CV) combined with quadrupole mass spectrometry (QMS) allows us to monitor methane formation online under high-temperature conditions (973 K, Figure 3). The bottom region of Figure 3 represents the chosen sequence of linear sweeps of the potential ( $E_{\text{WE}}$ , scan rate = 50 mV/s, blue trace) and the resulting current ( $I$ , pink trace) as a function of time. As the SOEC is operated in a single reactant gas atmosphere (i.e., no separated anode and cathode compartments), the QMS detects gaseous species produced by both electrode sides, which makes a distinction between products formed at the WE vs. CE necessary (possible anode reactions: oxidation of  $\text{CO}$ ,  $\text{H}_2$ , and/or already deposited, hydrogenation-inactive C to  $\text{CO}_2$ ,  $\text{H}_2\text{O}$ , or  $\text{CO}$ ). As mentioned above, the thermo-catalytic ground levels of the  $\text{CO}$  methanation rate are largely different on Ni(Cu) vs. Pt, and the contribution of the Pt side can be neglected. The potential was swept between  $-4$  V and  $+4$  V to generate high current densities and, thus, appropriate quantities of products for the QMS detection, both at the  $\text{Ni}_{80}\text{Cu}_{20}/8\text{-YSZ}$  WE and the Pt/GDC-10 CE (Figure 3B). In panel A, the CV sweeps were limited to a strong cathodic polarization of the WE only, in order to suppress superimposed QMS intensity via cathodic polarization of the CE. The time-dependent intensity changes of the  $\text{CH}_4$ -specific ( $m/z = 15$ ) signal measured during the sweeps can be directly correlated to the alternating potentials applied to the WE/CE (violet shaded area for the CE) and the respective electrolysis current changes. For details regarding QMS data analysis and  $I$  vs.  $E$  curves, we refer to the SI (Figure S4).

The main results derived from the data of Figure 3 are as follows:

- (a) On both the WE and the CE, the methanation reaction is promoted via cathodic polarization triggering reaction (3);
- (b) Ongoing reaction (6) suggests the contribution of a faradaic enhancement in activity on both electrodes via an increase in the surface carbon activity ( $a(\text{C})$ , compare equation (7));
- (c) Methane formation is much more promoted on the Pt/GDC-10 CE than on the WE, irrespective of Ni or  $\text{Ni}_{80}\text{Cu}_{20}$  being used as the metallic WE phase;
- (d) Methane promotion at the CE is associated with a much smaller charge transfer for the  $\text{CO}$  electrolysis reaction (3) as compared to the WE, suggesting a relatively higher efficiency in the hydrogenation of surface C;
- (e) The first cathodic polarization cycle of the CE yields no measurable  $\text{CH}_4$  formation but is expected to activate the CE for  $\text{CH}_4$  formation for the second cycle. It appears likely that the oxygen-ion buffering GDC requires sufficient oxygen-ion withdrawal in a first cycle to activate the TPB in terms of generating a proper oxygen vacancy concentration;
- (f) Once the CE is activated, the time-response of formation of additional  $\text{CH}_4$  from  $\text{C}_{\text{TPB}}$  is much faster on the CE, as deduced from the synchronicity of cathodic CE polarization and the accelerated  $\text{CH}_4$  increase;
- (g)  $\text{CH}_4$  formation on the WE starts immediately at the beginning of the first cathodic polarization cycle, but then increases rather slowly and is associated with a smaller amount of  $\text{CH}_4$  yielded from  $\text{C}_{\text{TPB}}$ , especially in view of the much larger integral

charge transfer. The response of  $\text{CH}_4$  formation to the alternating potential is very sluggish on the WE as compared to the CE.

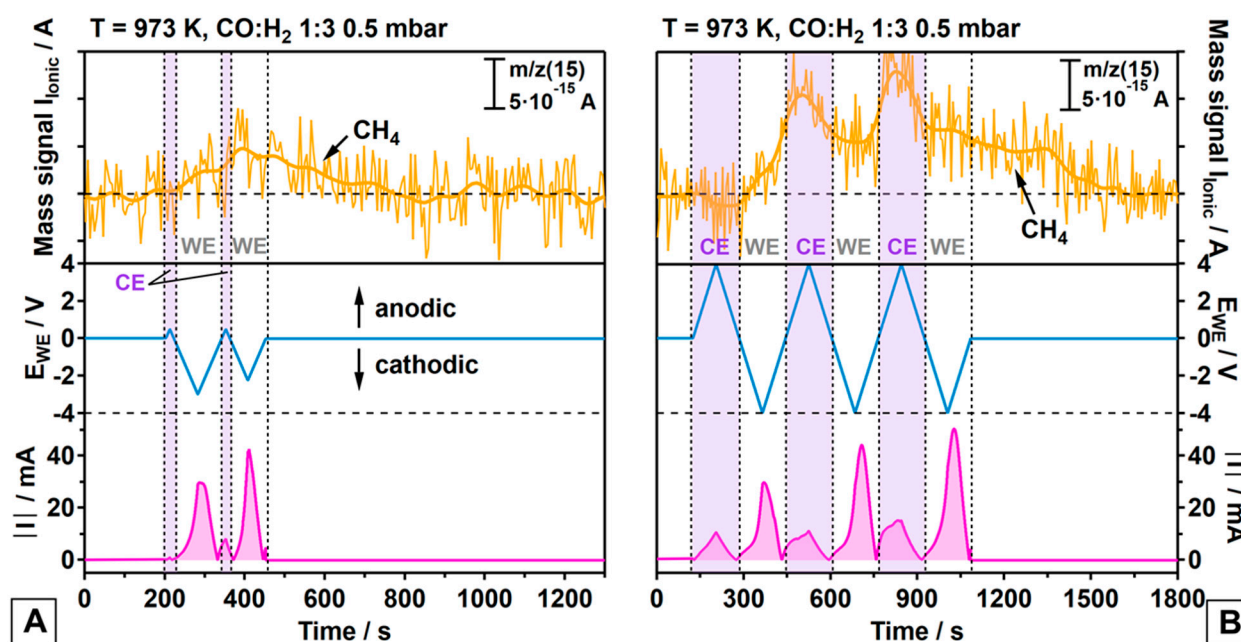


**Figure 3.** Top panels, light orange traces (raw and smoothed experimental data): electrochemically-promoted methane formation caused by alternating the cathodic polarizations of the WE vs. CE. (A): light blue traces: preferential cathodic polarization of  $\text{Ni}_{80}\text{Cu}_{20}/8\text{-YSZ}$  WE with max. 3V; (B): alternating polarization of WE and CE with max. 4V. The respective absolute current changes are shown in the bottom panels as pink traces. To highlight the alternating cathodic operation of the CE vs. WE and the time-correlated changes of the  $m/z = 15$  mass signal of  $\text{CH}_4$ , negative potentials at the CE are highlighted by a violet-shaded background.

The CO methanation results suggest that more  $\text{C}_{\text{TPB}}$  must have been formed electrochemically on  $\text{Ni}_{80}\text{Cu}_{20}/8\text{-YSZ}$  than on  $\text{Pt}/\text{GDC-10}$  but remains kinetically less reactive toward methane formation. Considering the strongly different properties of the WE and CE materials, it appears reasonable that less  $\text{C}_{\text{TPB}}$  accumulates on Pt in the presence of  $\text{H}_2$ , as carbon is bonded less strongly and is therefore more reactive toward  $\text{H}(\text{ads})$  on Pt relative to Ni. Moreover,  $\text{H}_2$  activation is highly efficient on the carbon-free Pt surface. The fact that the onset of  $\text{CH}_4$  formation is hardly delayed on the WE but needs a full cathodic activation cycle on the CE can be explained by the much higher oxygen exchange capacity of GDC in comparison to 8-YSZ. While any oxygen vacancy in 8-YSZ generated electrochemically at the WE side is immediately quenched by the splitting of CO toward lattice oxygen and  $\text{C}_{\text{TPB}}$ , GDC likely requires an enhanced reductive activation by withdrawing sufficient lattice oxygen before CO can become dissociated at the TPB.

#### 4. Conclusions

In summary, the oxidative de-coking reaction of pre-deposited  $\text{C}_{\text{TPB}}$  in the presence of  $\text{CO}_2$  ( $\text{C}_{\text{TPB}} + \text{CO}_2 \rightarrow 2 \text{CO}$ ) works more efficiently on  $\text{Ni}_{80}\text{Cu}_{20}$ , supporting its previously reported enhanced coking resilience in the presence of  $\text{CO}_2$  relative to clean Ni [16].

The original goal of this study, namely the quantitative distinction of the electrochemical enhancement of CO-methanation on clean Ni vs.  $\text{Ni}_{80}\text{Cu}_{20}$ , is not sufficiently reliable in view of the signal-to-noise ratio of the available QMS data. Ni/8-YSZ and  $\text{Ni}_{80}\text{Cu}_{20}/8\text{-YSZ}$  show almost indistinguishable  $\text{CH}_4$  formation properties, as shown in Figure S5 of the SI. These *operando* XPS measurements validate the accumulation of additional  $\text{C}_{\text{TPB}}$  only on  $\text{Ni}_{80}\text{Cu}_{20}/8\text{-YSZ}$  during the chronoamperometric experiments in a  $\text{CO}/\text{H}_2$  atmosphere

at  $-1.25$  V, whereas on Ni/8-YSZ, no  $C_{TPB}$  is visible at  $-1.00$  V. However, the methane QMS signal ( $m/z = 15$ ) increases similarly on both electrodes until the polarization is turned off. Based on the carbon dissolution properties (Ni > NiCu) and  $H_{ads}$  kinetics (Ni > NiCu), and together with results shown in Figure 2 and Figure S5, it can be concluded that on pure Ni/8-YSZ, electrochemically-induced C atoms at the TBP (i) become hydrogenated to  $CH_4$  and (ii) are more easily dissolved in the Ni bulk and, therefore, do not accumulate at the surface, which can explain why they are not spectroscopically detectable. Figures S6 and S7 provide evidence for the metallic state of Ni and Cu anticipated under strongly reductive  $CO/H_2$  conditions. Together with the O1s region, no significant redox changes of Ni or Cu in the XP-spectra upon polarization (OCP vs.  $-1.25$  V) were detected. Essentially, one would expect NiCu to be a poorer thermal/non-electrochemical CO and/or  $CO_2$  methanation catalyst than pure Ni [18–20], but it remains unclear whether a specific superposition of faradaic and non-faradaic (EPOC) promotional effects can revert this trend. The preferential coking of NiCu under cathodic polarization in  $CO/H_2$  represents a hint for a delayed reaction of  $C_{TPB}$  toward  $CH_4$ , suggesting that NiCu offers little, if any, advantages relative to pure Ni. Whether the electrochemically-induced adsorbate and carbon chemistry affects the local Cu/Ni segregation behavior, and therefore alter the associated gas–surface interactions [29], remains open too, and calls for non-porous model electrode systems.

Nevertheless, the remaining central message of this work refers to the appropriate choice of materials in creating a (bi)metal–mixed oxide electrolyte interface for optimized thermodynamic enhancement of  $CH_4$  yield. The combination of reactive  $C_{TPB}$  and high  $H(ads)$  coverages on the metallic component with suppressed coking and superior properties of the metal–electrolyte interface for C–O bond activation is the key for electrochemical enhancement of the  $CH_4$  yield in the co-electrolysis of  $CO_2$  and water via intermediate CO and  $H_2$ . Obviously, these prerequisites are better matched with Pt/GDC than by Ni(Cu)/YSZ.

**Supplementary Materials:** The following supporting information can be downloaded at: <https://www.mdpi.com/article/10.3390/c9040106/s1>, Figure S1: SOEC cell preparation, sample mounting, equipment and XPS data analysis, Figure S2: XPS comparison of Ni/8-YSZ vs.  $Ni_{80}Cu_{20}/8-YSZ$  upon carbon accumulation, Figure S3: Thermodynamic promotion of  $CH_4$  formation, Figure S4: QMS data analysis and Cyclovoltammetry I vs. E curves, Figures S5–S7: Operando XPS comparison of Ni/8-YSZ vs.  $Ni_{80}Cu_{20}/8-YSZ$  in  $CO/H_2$  atmosphere.

**Author Contributions:** Conceptualization, B.K. and C.W.T.; methodology, C.W.T., L.H., D.W. (Daniel Winkler); software, T.G., E.C.; validation, T.G., E.C., J.K.-L., E.P., S.P., and B.K.; formal analysis, C.W.T., L.H., D.W. (Daniel Werner); investigation, M.T., C.W.T., L.H., D.W. (Daniel Winkler), C.G., M.L., D.W. (Daniel Werner), T.M., L.A.S. and B.K.; resources, B.K.; data curation, C.W.T.; writing—original draft preparation, C.W.T.; writing—review and editing, B.K. and C.W.T.; visualization, C.W.T. and E.P.; supervision, B.K.; project administration, B.K.; funding acquisition, B.K. and E.P. All authors have read and agreed to the published version of the manuscript.

**Funding:** Financial support was provided by the research platform “Materials- and Nanoscience” and the special PhD program “Reactivity and Catalysis” at the University of Innsbruck. C.W.T. acknowledges a PhD position via doctoral program “Reactivity and Catalysis” of the University of Innsbruck. Additionally, L.H. and C.G. acknowledge funding by the Austrian Research Promotion Agency (FFG) via project 870523, and D.W. is a recipient of a DOC Fellowship of the Austrian Academy of Sciences at the Department of Physical Chemistry. E.P. acknowledge funding by the Austrian Research Promotion Agency (FFG) via project 877095 and by the Austrian Science Fund (FWF) via project P34233 and P35510.

**Data Availability Statement:** The data presented in this study are available on request from the corresponding author.

**Acknowledgments:** The Helmholtz Zentrum Berlin für Materialien und Energie, BESSY II, is acknowledged for the allocation of the beamtime to proposal number 202-09705-ST-1.1-P.

**Conflicts of Interest:** The authors declare no conflict of interest.

## References

1. Zheng, Y.; Wang, J.; Yu, B.; Zhang, W.; Chen, J.; Qiao, J.; Zhang, J. A review of high temperature co-electrolysis of H<sub>2</sub>O and CO<sub>2</sub> to produce sustainable fuels using solid oxide electrolysis cells (SOECs): Advanced materials and technology. *Chem. Soc. Rev.* **2017**, *46*, 1427–1463. [[CrossRef](#)] [[PubMed](#)]
2. Li, W.; Wang, H.; Shi, Y.; Cai, N. Performance and methane production characteristics of H<sub>2</sub>O–CO<sub>2</sub> co-electrolysis in solid oxide electrolysis cells. *Int. J. Hydrogen Energy* **2013**, *38*, 11104–11109. [[CrossRef](#)]
3. Gao, J.; Wang, Y.; Ping, Y.; Hu, D.; Xu, G.; Gu, F.; Su, F. A thermodynamic analysis of methanation reactions of carbon oxides for the production of synthetic natural gas. *RSC Adv.* **2012**, *2*, 2358–2368. [[CrossRef](#)]
4. Vayenas, C.G.; Bebelis, S.; Neophytides, S. Non-Faradaic electrochemical modification of catalytic activity. *J. Phys. Chem.* **1988**, *92*, 5083–5085. [[CrossRef](#)]
5. Katsaounis, A. Recent developments and trends in the electrochemical promotion of catalysis (EPOC). *J. Appl. Electrochem.* **2010**, *40*, 885–902. [[CrossRef](#)]
6. Imbihl, R. Electrochemical promotion of catalytic reactions. *Prog. Surf. Sci.* **2010**, *85*, 241–278. [[CrossRef](#)]
7. Bebelis, S.; Karasali, H.; Vayenas, C.G. Electrochemical promotion of CO<sub>2</sub> hydrogenation on Rh/YSZ electrodes. *J. Appl. Electrochem.* **2008**, *38*, 1127–1133. [[CrossRef](#)]
8. Giehr, A.; Maier, L.; Schunk, S.A.; Deutschmann, O. Thermodynamic Considerations on the Oxidation State of Co/ $\gamma$ -Al<sub>2</sub>O<sub>3</sub> and Ni/ $\gamma$ -Al<sub>2</sub>O<sub>3</sub> Catalysts under Dry and Steam Reforming Conditions. *ChemCatChem* **2018**, *10*, 751–757. [[CrossRef](#)]
9. Pakhare, D.; Spivey, J. A review of dry (CO<sub>2</sub>) reforming of methane over noble metal catalysts. *Chem. Soc. Rev.* **2014**, *43*, 7813–7837. [[CrossRef](#)]
10. Degerman, D.; Lömker, P.; Goodwin, C.M.; Shipilin, M.; García-Martínez, F.; Schlueter, C.; Nilsson, A.; Amann, P. State of the Surface During CO Hydrogenation over Ni(111) and Ni(211) Probed by Operando X-ray Photoelectron Spectroscopy. *J. Phys. Chem. C* **2023**, *127*, 4021–4032. [[CrossRef](#)]
11. Chen, Y.; Zhang, Y.; Lin, Y.; Yang, Z.; Su, D.; Han, M.; Chen, F. Direct-methane solid oxide fuel cells with hierarchically porous Ni-based anode deposited with nanocatalyst layer. *Nano Energy* **2014**, *10*, 1–9. [[CrossRef](#)]
12. Qu, J.; Wang, W.; Chen, Y.; Deng, X.; Shao, Z. Stable direct-methane solid oxide fuel cells with calcium-oxide-modified nickel-based anodes operating at reduced temperatures. *Appl. Energy* **2016**, *164*, 563–571. [[CrossRef](#)]
13. An, W.; Zeng, X.C.; Turner, C.H. First-principles study of methane dehydrogenation on a bimetallic Cu/Ni(111) surface. *J. Chem. Phys.* **2009**, *131*, 174702. [[CrossRef](#)] [[PubMed](#)]
14. Song, K.; Lu, M.; Xu, S.; Chen, C.; Zhan, Y.; Li, D.; Au, C.; Jiang, L.; Tomishige, K. Effect of alloy composition on catalytic performance and coke-resistance property of Ni-Cu/Mg(Al)O catalysts for dry reforming of methane. *Appl. Catal. B* **2018**, *239*, 324–333. [[CrossRef](#)]
15. An, W.; Gatewood, D.; Dunlap, B.; Turner, C.H. Catalytic activity of bimetallic nickel alloys for solid-oxide fuel cell anode reactions from density-functional theory. *J. Power Sources* **2011**, *196*, 4724–4728. [[CrossRef](#)]
16. Zambaldi, P.; Haug, L.; Penner, S.; Klötzer, B. Dry Reforming of Methane on NiCu and NiPd Model Systems: Optimization of Carbon Chemistry. *Catalysts* **2022**, *12*, 311. [[CrossRef](#)]
17. Lee, G.-J.; Lee, J.-H.; Lee, D.; Park, K.-I.; Jeong, C.K.; Park, J.-J.; Lee, M.-K. Synthesis and characterization of carbon-coated Cu-Ni alloy nanoparticles and their application in conductive films. *Appl. Surf. Sci.* **2021**, *566*, 150672. [[CrossRef](#)]
18. Luyten, L.J.M.; Von Eck, M.; Von Grondelle, J.; Von Hooff, J.H.C. Hydrogenation of carbon monoxide over silica supported nickel-copper and ruthenium-copper catalysts. *J. Phys. Chem.* **1978**, *82*, 2000–2002. [[CrossRef](#)]
19. Hatta, A.H.; Jalil, A.A.; Hassan, N.S.; Hamid, M.Y.S.; Rahman, A.F.A.; Teh, L.P.; Prasetyoko, D. A review on recent bimetallic catalyst development for synthetic natural gas production via CO methanation. *Int. J. Hydrogen Energy* **2022**, *47*, 30981–31002. [[CrossRef](#)]
20. Tsiotsias, A.I.; Charisiou, N.D.; Yentekakis, I.V.; Goula, M.A. Bimetallic Ni-Based Catalysts for CO<sub>2</sub> Methanation: A Review. *Nanomaterials* **2021**, *11*, 28. [[CrossRef](#)]
21. Schmider, D.; Maier, L.; Deutschmann, O. Reaction Kinetics of CO and CO<sub>2</sub> Methanation over Nickel. *Ind. Eng. Chem. Res.* **2021**, *60*, 5792–5805. [[CrossRef](#)]
22. Wensheng, X.; Haiyou, W.; Huilin, W.; Qianer, Z. An energetics study on syngas(CO+H<sub>2</sub>) methanation reaction on Ni, Cu and Ni-Cu alloy surfaces by bond-order conservation model. *Acta Chim. Sinica* **1998**, *56*, 773–779.
23. Luo, Y.; Li, W.; Shi, Y.; Ye, X.; Wang, S.; Cai, N. Methane Synthesis Characteristics of H<sub>2</sub>O/CO<sub>2</sub> Co-Electrolysis in Tubular Solid Oxide Electrolysis Cells. *ECS Trans.* **2015**, *68*, 3465. [[CrossRef](#)]
24. Fleig, J.; Baumann, F.S.; Brichzin, V.; Kim, H.R.; Jamnik, J.; Cristiani, G.; Habermeier, H.U.; Maier, J. Thin Film Microelectrodes in SOFC Electrode Research. *Fuel Cells* **2006**, *6*, 284–292. [[CrossRef](#)]
25. Vannice, M.A. The catalytic synthesis of hydrocarbons from H<sub>2</sub>CO mixtures over the group VIII metals: II. The kinetics of the methanation reaction over supported metals. *J. Catal.* **1975**, *37*, 462–473. [[CrossRef](#)]
26. Barbieri, P.F.; de Siervo, A.; Carazzolle, M.F.; Landers, R.; Kleiman, G.G. XPS and XAES study of Ag–Pd and Cu–Ni alloys: Spectra, shifts and electronic structure information. *J. Electron. Spectrosc. Relat. Phenom.* **2004**, *135*, 113–118. [[CrossRef](#)]
27. Biesinger, M.C. Advanced analysis of copper X-ray photoelectron spectra. *Surf. Interface Anal.* **2017**, *49*, 1325–1334. [[CrossRef](#)]
28. Biesinger, M.C. Accessing the robustness of adventitious carbon for charge referencing (correction) purposes in XPS analysis: Insights from a multi-user facility data review. *Appl. Surf. Sci.* **2022**, *597*, 153681. [[CrossRef](#)]

29. Zegkinoglou, I.; Pielsticker, L.; Han, Z.-K.; Divins, N.J.; Kordus, D.; Chen, Y.-T.; Escudero, C.; Pérez-Dieste, V.; Zhu, B.; Gao, Y.; et al. Surface Segregation in CuNi Nanoparticle Catalysts During CO<sub>2</sub> Hydrogenation: The Role of CO in the Reactant Mixture. *J. Phys. Chem. C* **2019**, *123*, 8421–8428. [[CrossRef](#)]
30. Linstrom, P. *NIST Chemistry WebBook, NIST Standard Reference Database 69*; National Institute of Standards and Testing (NIST): Gaithersburg, MD, USA, 1997. [[CrossRef](#)]

**Disclaimer/Publisher's Note:** The statements, opinions and data contained in all publications are solely those of the individual author(s) and contributor(s) and not of MDPI and/or the editor(s). MDPI and/or the editor(s) disclaim responsibility for any injury to people or property resulting from any ideas, methods, instructions or products referred to in the content.